metals

MDPI

Article

The Microstructure, Tensile and Impact Properties of Low-Activation Ferritic-Martensitic Steel EK-181 after High-Temperature Thermomechanical Treatment

Nadezhda Polekhina [1,*], Valeria Linnik [1], Igor Litovchenko [1], Kseniya Almaeva [1], Sergey Akkuzin [1], Evgeny Moskvichev [1], Vyacheslav Chernov [2], Mariya Leontyeva-Smirnova [2], Nikolay Degtyarev [2] and Kirill Moroz [2]

[1] Institute of Strength Physics and Materials Science SB RAS, 2/4 Pr. Akademicheskii, 634055 Tomsk, Russia
[2] JSC "A. A. Bochvar High-Technology Research Institute of Inorganic Materials", 5 Rogov St., 123060 Moscow, Russia
* Correspondence: nadejda89tsk@yandex.ru; Tel.: +7-923-421-47-37

Abstract: In this work, we study the effect of high-temperature thermomechanical treatment (HTMT) with deformation in the austenite region on the microstructure, tensile properties, impact toughness, and fracture features of advanced low-activation 12% chromium ferritic-martensitic reactor steel EK-181. HTMT more significantly modifies the steel structural-phase state than the traditional heat treatment (THT). As a result of HTMT, the hierarchically organized structure of steel is refined. The forming grains and subgrains are elongated in the rolling direction and flattened in the rolling plane (so-called pancake structure) and have a high density of dislocations pinned by stable nanosized particles of the MX type. This microstructure provides a simultaneous increase, relative to THT, in the yield strength and impact toughness of steel EK-181 and does not practically change its ductile-brittle transition temperature. The most important reasons for the increase in impact toughness are a decrease in the effective grain size of steel (martensite blocks and ferrite grains) and the appearance of a crack-arrester type delamination perpendicular to the main crack propagation direction. This causes branching of the main crack and an increase in the absorbed impact energy.

Keywords: ferritic-martensitic steel EK-181; microstructure; mechanical properties; ductile-brittle transition temperature; impact toughness; fracture; delamination; high temperature thermomechanical treatment

Citation: Polekhina, N.; Linnik, V.; Litovchenko, I.; Almaeva, K.; Akkuzin, S.; Moskvichev, E.; Chernov, V.; Leontyeva-Smirnova, M.; Degtyarev, N.; Moroz, K. The Microstructure, Tensile and Impact Properties of Low-Activation Ferritic-Martensitic Steel EK-181 after High-Temperature Thermomechanical Treatment. *Metals* **2022**, *12*, 1928. https://doi.org/10.3390/met12111928

Academic Editor: Beatriz López Soria

Received: 21 October 2022
Accepted: 9 November 2022
Published: 10 November 2022

1. Introduction

At present, high-temperature low-activation 12% Cr ferritic-martensitic steels are considered as priority structural materials for the core of Generation IV reactors. Their advantages over the austenitic steels are high resistance to radiation swelling and helium embrittlement, high thermal conductivity, low thermal expansion coefficient, and high corrosion resistance in liquid metal coolants [1–6].

The requirements for steels of this class are high heat resistance and reduced tendency to cold embrittlement. To expand the range of operating temperatures of ferritic-martensitic steels, it is necessary to modify their microstructure, which provides a simultaneous increase in high-temperature mechanical properties and does not adversely affect the position of the ductile-brittle transition temperature (DBTT). An additional limitation is associated with a shift of DBTT of steels towards higher temperatures during radiation exposure [7–9]. In this case, the initial microstructure of the material affects the value of this displacement.

Commonly, heat-resistant ferritic-martensitic steels are complexly alloyed dispersion-hardened materials [1,5,7,10–13]. Their traditional heat treatment (THT) includes normalization (at $T \geq 1050$ °C) and high (at $T \geq 700$ °C) tempering. As a result of THT, a tempered ferritic-martensitic microstructure is formed with particles of the second phases: relatively coarse (from tens to hundreds of nanometers) carbides $M_{23}C_6$ (M–Cr, Mn, Fe, W, etc.) and

nanosized (up to 10–15 nm) carbonitrides of the MX type (M–V, Ti, Ta, Nb, Mo, etc., X–C, N) [14–17]. The $M_{23}C_6$ carbides are usually located at the grain and subgrain boundaries. The MX carbonitrides lie inside the martensite laths and ferrite grains.

One of the well-known and widely used ways to simultaneously increase the yield strength and toughness of steels is to reduce the size of their structural elements [18–20]. For that purpose, various modes of high-temperature thermomechanical treatment (HTMT) of steels with a BCC (body-centered cubic) lattice, including the high-chromium ferritic-martensitic reactor steels, are being actively developed [7,10–13,17,20]. The main idea of HTMT with deformation in the austenitic region (ausforming) is to refine the martensitic structure by reducing the grain size of the prior austenite and increasing the volume fraction of fine particles of the MX type, which pin the dislocation structure of the steel [5,6,8,10–14,16,21].

According to [6,10,13,14,16], the MX carbonitride nanoparticles have a high thermal stability during long-term aging and creep. Pinning dislocations, they inhibit the material microstructure degradation at high temperatures [5,14,21,22]. It is also reported [6,16] that the rate of coarsening of $M_{23}C_6$ carbides during creep is much higher than that of precipitates of the MX phase. The value of dispersion strengthening by the second phase particles is determined by their size, volume fraction (density), shape, features of spatial distribution and composition. In this regard, in addition to considering the factors responsible for grain-boundary hardening (refining of the martensitic structure) of steels, special attention is paid to their carbide subsystem.

It is reported [5,8,11,23,24] that HTMT makes it possible to increase the strength properties of ferritic-martensitic steels both at room and at elevated test temperatures (T = 600–650 °C) and has a positive effect on their creep resistance [6,16]. However, this treatment can lead to the formation of an anisotropic microstructure [18,22,23]. It causes the dependence of the mechanical properties on the sample orientation relative to the direction and plane of rolling.

In [17,25,26], the efficiency of applying HTMT to 12% chromium ferritic-martensitic steels EK-181 and EP-823 is shown. It has been established [25,26] that HTMT according to the proposed modes increases (by ≈ 20%) their strength characteristics in a wide temperature range from −196 to 700 °C without a significant decrease in plasticity. In view of the above requirements for the materials under consideration, it is necessary to comprehensively study their microstructural parameters after HTMT in combination with the strength, plasticity, and impact properties in a wide temperature range.

In this paper, the effect of HTMT on the features of the heterophase, defective microstructure of low-activation ferritic-martensitic steel EK-181 (Fe-12Cr-2W-V-Ta-B) is studied in detail, the relationship between microstructural parameters and its strength, impact properties and fracture patterns is discussed at different temperatures, including the region of ductile-brittle transition.

2. Materials and Methods

The elemental composition of the EK-181 steel is presented in Table 1. Traditional heat treatment (THT) includes air quenching from T = 1100 °C (holding for 1 h) and tempering at T = 720 °C (holding for 3 h).

Table 1. Elemental composition of EK-181 steel (wt.%, base Fe).

C	Cr	Mn	Mo	Nb	V	W	Ni	N	Si	Ta	Ce	Ti	B	Zr
0.16	11.17	0.74	0.01	0.01	0.25	1.13	0.03	0.04	0.33	0.08	0.15	0.05	0.006	0.05

High-temperature thermomechanical treatment (HTMT) was carried out according to the following regime (Figure 1a): heating to T = 1100 °C (with holding for 1 h) + hot plastic deformation by rolling in the austenite phase to a value of ε ≈ 50% (the rolls of the rolling mill were at room temperature) + quenching in water + tempering at 720 °C (exposure 1 h).

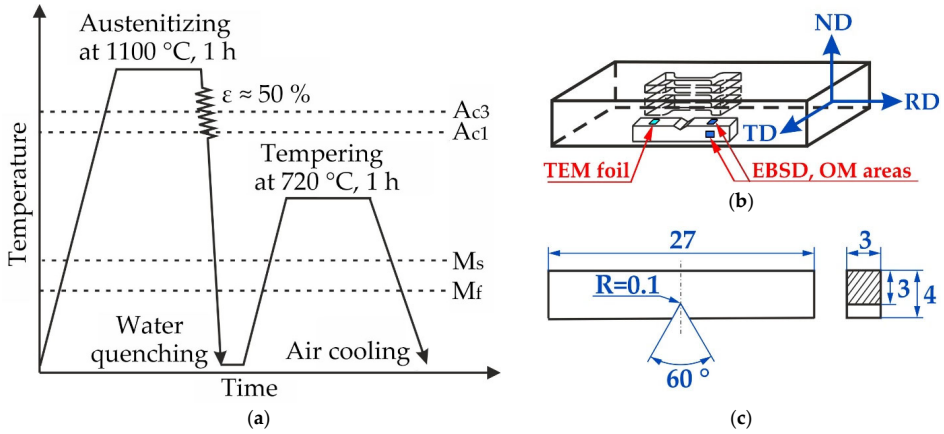

Figure 1. Scheme of high-temperature thermomechanical treatment of steel EK-181 (**a**), scheme of a small (KLST) sample for testing impact strength (**b**), scheme of cutting of the samples after HTMT with respect to the direction and plane of rolling (**c**). Sample dimensions are given in mm. RD is the rolling direction, ND is the direction normal to the rolling plane, TD is the transverse direction.

Metallographic studies in the TD-RD and ND-RD sections (where RD is the rolling direction, ND is the direction normal to the rolling plane, TD is the transverse direction, Figure 1b) were carried out using an Olympus GX71 optical microscope (OM, OLYMPUS Corporation, Tokyo, Japan). Etching of the samples to reveal the boundaries of the prior austenite grains and particles of the second phases was carried out using a Vilella's reagent (5 mL HCl, 1 g picric acid, 100 mL ethanol).

The steel grain-subgrain microstructure, the second phase particle composition and morphology, and the features of their distribution were studied by scanning electron microscopy (SEM) on a Tescan MIRA 3 LMU microscope (TESCAN ORSAY HOLDING, Brno, Czech Republic) with a field emission gun (FEG). It is equipped with a detector of backscattered electrons (Electron Backscatter Diffraction, EBSD) Oxford Instruments Nordlys F (Oxford Instruments, High Wycombe, UK) and an X-ray energy dispersive X-ray (EDX) microanalysis system with an Ultim MAX 40 detector.

The samples for the SEM EBSD studies were prepared by mechanical polishing followed by ion treatment using a Technoorg Linda SEMPrep 2 system (Technoorg Linda Co. Ltd., Budapest, Hungary) as the final polishing step. After HTMT, the studies were carried out in a section parallel to the rolling plane (TD-RD plane) and in a cross section (ND-RD plane, Figure 1b). The accelerating voltage was 15 kV, the scanning step was 150 nm. Microstructural analysis was performed using Oxford Instruments Aztec software (version 3.1, Oxford Instruments, High Wycombe, UK). The boundaries with a misorientation angle of $2^\circ < \theta \leq 15^\circ$ were taken to be low-angle boundaries (LABs) (boundaries with a misorientation of $< 2^\circ$ were not taken into account). The boundaries with a misorientation angle $\theta > 15^\circ$ were considered to be high-angle boundaries (HABs).

The grain size was determined as the value of the equivalent circle diameter (ECD) with high-angle boundaries. In the steel under study, this parameter correlates with the sizes of martensite blocks and ferrite grains, since they are the smallest structural units separated from each other mainly by high-angle boundaries.

The mechanical tensile tests were carried out at a strain rate of $\approx 2 \times 10^{-3}$ s^{-1} on a testing machine of the Polyani type NIKIMT 1246R-2/2300 (NIKIMP, Moscow, Russia). In the study at negative temperatures, the samples were deformed in a mixture of liquid nitrogen and ethanol. The tests at room and elevated temperatures were carried out in vacuum $\approx 2.7 \times 10^{-3}$ Pa. We used dogbone-shaped samples with a gage section of 13.0 × 2.0 × 1.0 mm. The scheme of cutting samples from rolled sheets is shown in Figure 1b.

The serial tests for impact strength were carried out on small (KLST, standard NF EN ISO 14556) Charpy-type samples (with a 1 mm deep V-shaped notch with a notch tip

radius of R = 0.1 mm, Figure 1c) in the temperature range −186–100 °C on the pendulum impact tester PSd 450 (WPM Werkstoffprufsysteme Leipzig GmbH, Leipzig, Germany). The samples after HTMT were cut along the rolling direction (RD) as shown in Figure 1b. The direction of the pendulum impact was parallel to the direction normal to the rolling plane (ND). At each temperature three samples were tested. The ductile-brittle transition temperature (DBTT) was determined as the midpoint between the maximum and minimum impact strength values in the studied temperature range.

The transmission electron microscopy (TEM) studies were carried out on a JEOL JEM-2100 microscope (JEOL Ltd., Tokyo, Japan) accelerating voltage 200 kV) equipped with an X-ray energy dispersive microanalysis system (INCA Energy microanalyzer, Oxford Instruments, High Wycombe, UK). Thin foils were prepared from a section parallel to the rolling plane (TD-RD, Figure 1b) by electrolytic polishing in a solution of chromic anhydride (CrO_3, 50 g) in phosphoric acid (H_3PO_4, 450 mL). The dislocation density was calculated by the secant method from bright-field and dark-field electron microscopy images. The average transverse dimensions of martensite laths and the sizes (diameter) of particles of carbide (carbonitride) phases were also estimated.

The fracture surfaces of the samples after the impact tests were studied by scanning electron microscopy using a Tescan MIRA 3 LMU microscope (TESCAN ORSAY HOLDING, Brno, Czech Republic). The fractions of the ductile and brittle components in the fractures of the samples tested at different temperatures were calculated according to the ASTM E23-05 standard. The fracture appearance transition temperature (FATT) was defined as the temperature at which the brittle fracture fraction reaches ≈50%.

3. Results

3.1. Optical Metallography

Figure 2 shows the optical images of etched sections of steel EK-181 after traditional heat treatment and high-temperature thermomechanical treatment in a section parallel to the rolling plane (TD-ND) and a transverse (TD-RD) section.

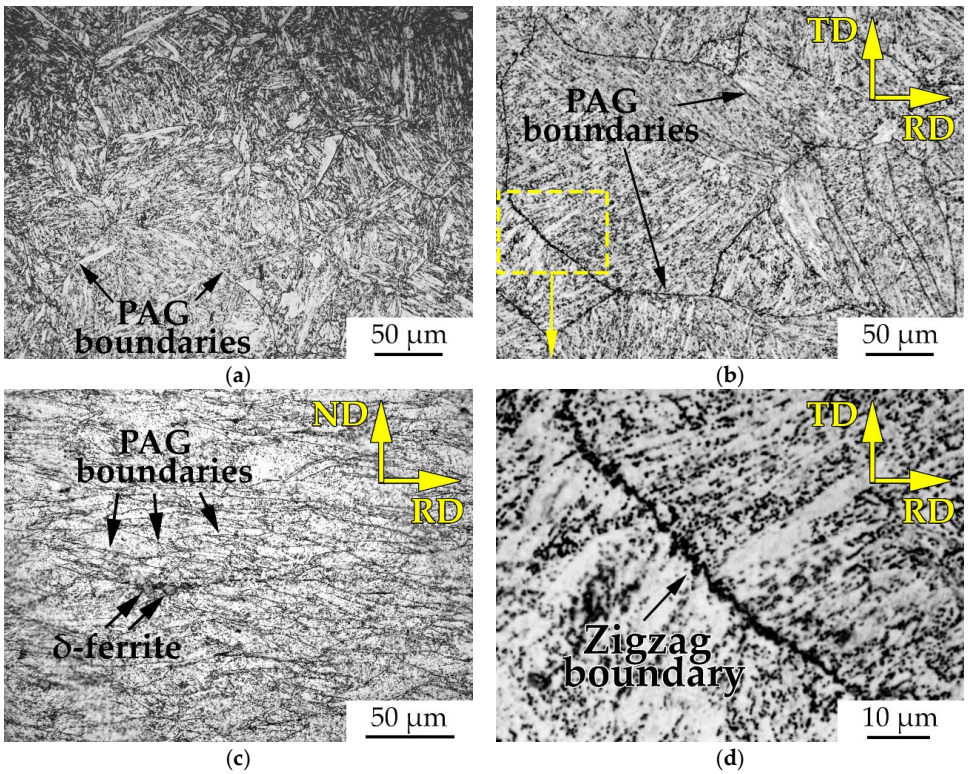

Figure 2. Optical micrograph of the steel EK-181 microstructure after THT (**a**) and HTMT (**b**–**d**): **b**, **d**—section parallel to the rolling plane, **c**—cross section.

As can be seen from this figure, after THT and HTMT (TD-ND section), a typical lath martensite structure is formed (Figure 2a,b) with a high density of misorientation boundaries. It is known [27,28] that in the ferritic-martensitic steels, such structures contain a whole hierarchy of structural elements (Figure 3). Figure 2a,b show the grain boundaries of the prior austenite (PAG), inside which martensite packets are located. The packets, in turn, consist of a group of blocks with almost the same habit plane. Finally, the blocks contain the laths of martensite having a close orientation and regions of α-ferrite. It is believed [18] that the boundaries of PAG, the packets and blocks of martensite, as well as ferrite grains are predominantly high-angle, and the boundaries of laths are low-angle.

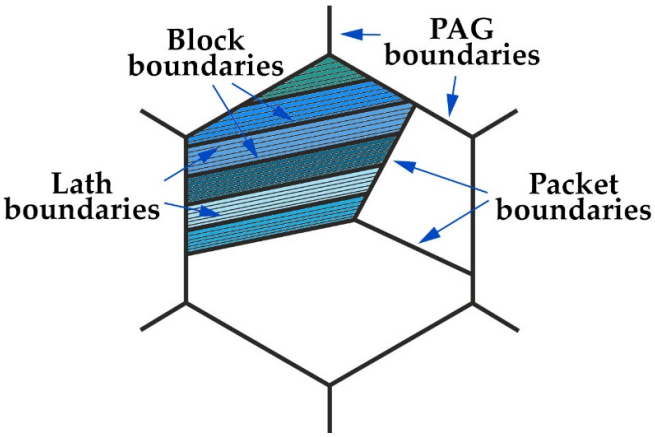

Figure 3. Scheme of lath martensitic structure.

After THT, the grains of the prior austenite have an almost equiaxed shape (Figure 2a). Their sizes range from ≈12 to 233 μm. The average size is 100 μm.

After HTMT, the boundaries of the relatively equiaxed prior austenite grains are also observed in the longitudinal section. However, there is a noticeable increase in the size of the PAG (Figure 2b), compared with the THT. In this section, their average size (diameter) is about 128 μm.

Another difference in the state after HTMT is the presence of parallel boundaries inside the grains of the prior austenite, which in most cases intersect the entire grain. It is assumed that these boundaries are the boundaries of twins, formed during the hot deformation of the austenite, remaining in the steel microstructure after martensitic transformation. In addition, quite often there are sections of the boundaries of the PAG of a zigzag type (Figure 2d). Its formation, in our opinion, is also caused by the processes of plastic deformation of the steel in the austenitic region.

When considering the microstructure of the steel after HTMT in the transverse (TD-RD) section (Figure 2c), it is clear that the PAG is extended along the rolling direction and flattened in the direction normal to the rolling plane. That is, non-equiaxed grains are formed with an average length of ≈67 μm and a width of ≈15 μm.

Also, the areas containing traces of globular δ-ferrite several (4–8) μm in size were found (Figure 2c). However, the volume fraction of this phase does not exceed ≈1.5%.

3.2. Scanning Electron Microscopy of Etched Sections

Scanning electron microscopy investigations of the etched sections of the steel after THT and HTMT showed (Figure 4) that after both treatments, the second phase particles have submicron sizes and are located mainly along the boundaries of structural elements (not in the grain body). They are observed both at the boundaries of prior austenite grains and at the boundaries of packets, blocks and martensite laths (Figure 4).

In accordance with the data of a local elemental energy-dispersive X-ray microanalysis (EDX, Figure 5b,c), the detected particles are carbides based on Cr–$M_{23}C_6$, which may also contain Fe, Mn, W, Si and other elements.

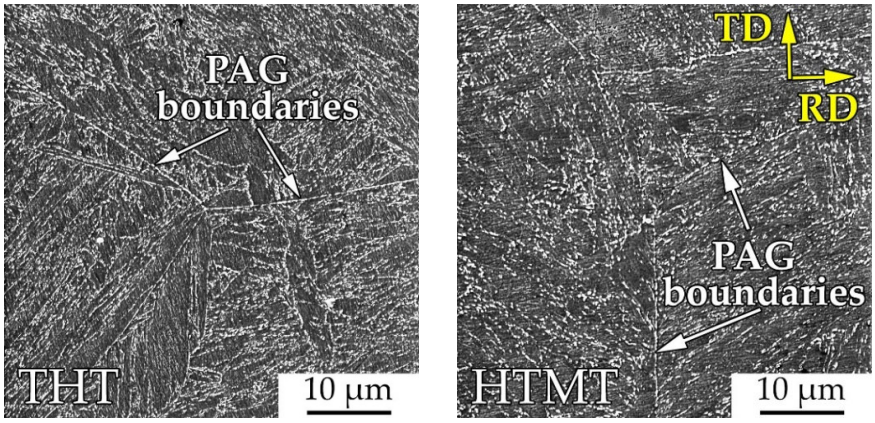

(**a**) (**b**)

Figure 4. SEM SE (secondary electrons) images of the etched surface of EK-181 steel samples after THT (**a**) and HTMT in a section parallel to the rolling plane (**b**).

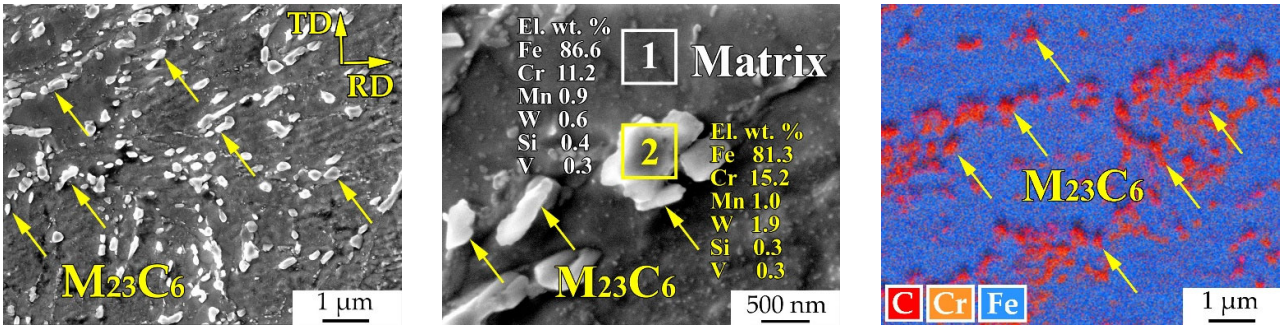

(**a**) (**b**) (**c**)

Figure 5. $M_{23}C_6$ carbides in EK-181 steel after HTMT: SEM SE images (**a**,**b**), EDX elemental map (**c**).

After THT, the average size of such particles is ≈ 250 nm (Figure 4). Their volume fraction, estimated from the area they occupy in SEM images, reaches ≈ 6.2%.

HTMT leads to a decrease in the average size of $M_{23}C_6$ carbides to ≈ 200 nm (Figures 4 and 5). At the same time, their volume fraction decreases to ≈ 5.4%.

Note that during the SEM study of the second phase particles on the etched surface of the steel, it is necessary to take into account the features of sample preparation. In particular, during selective etching, not all particles may be detected; some of them may fall out of the matrix into the etchant. Moreover, nanosized (a few to tens of nanometers) precipitates are difficult to distinguish. On the other hand, the contrast on the etched particles may contain larger areas, including some fragments of the matrix. This may lead to an overestimation of the volume fraction of the detected second phase precipitates [25].

3.3. EBSD-Investigation

Figure 6 shows the EBSD maps of EK-181 steel after THT and HTMT in two (TD-RD and ND-RD) sections. The results of the EBSD study are consistent with the optical metallography data. In addition, they make it possible to quantify the parameters of the steel substructure.

On the EBSD phase maps (Figure 6a–c) for both studied states, only the matrix phase (α-Fe, colored in blue) is displayed. With the selected scanning step (150 nm), even the most coarsely dispersed (tens to hundreds of nm in size) precipitates of the second phase particles (most of which are particles based on chromium—$M_{23}C_6$) are not resolved due to their relatively small (submicron) sizes and the similarity of their elemental composition to that of the matrix.

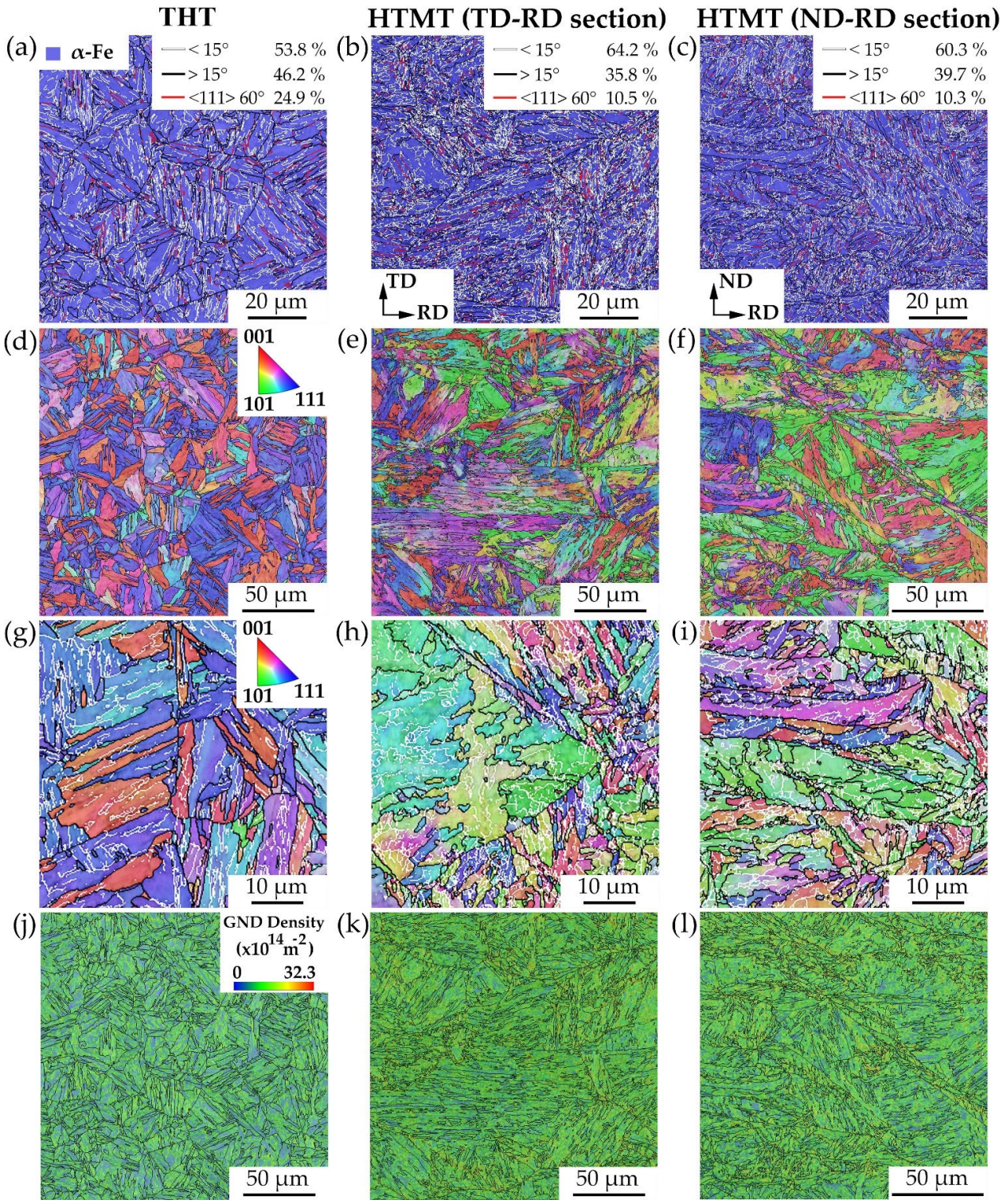

Figure 6. SEM EBSD images of steel microstructure after THT (**a**,**d**,**g**,**j**), HTMT in the section, parallel to the rolling plane (**b**,**e**,**h**,**k**), and in the cross section (**c**,**f**,**i**,**l**). Phase maps (**a**–**c**), where BCC-Fe is in blue color. IPF (Inverse Pole Figures) orientation maps (**d**–**i**), corresponding GND (Geometrically Necessary Dislocations) maps (**j**–**l**). High-, low-angle, and twin boundaries denoted by black, white and red lines, respectively.

As discussed above (Section 3.1, Figures 2 and 3), the steel under study clearly shows a hierarchy of its crystallographic units. From the inverse pole figures (IPF) orientation maps (Figure 6d–i) it can be seen that inside the grains of the prior austenite there are

areas with a slightly changing color shade, separated from the areas with a noticeably different orientation (different coloring) mainly by high-angle boundaries. Such regions are martensite blocks, combined into packets, and ferrite regions. The martensitic lamellas inside the blocks have a similar orientation and are separated from each other by low-angle boundaries (Figure 6d–i). After HTMT, low-angle boundaries might also be the boundaries of subgrains formed as a result of plastic deformation.

Figure 7 presents the statistical data of the EBSD analysis. It can be seen from the grain size distribution that, both after THT and after HTMT, the majority of structural elements separated by high-angle (>15°) boundaries have sizes of less than 5 μm (Figure 7a–c). There are only single grains up to several tens (≈ 40–50) of micrometers in size.

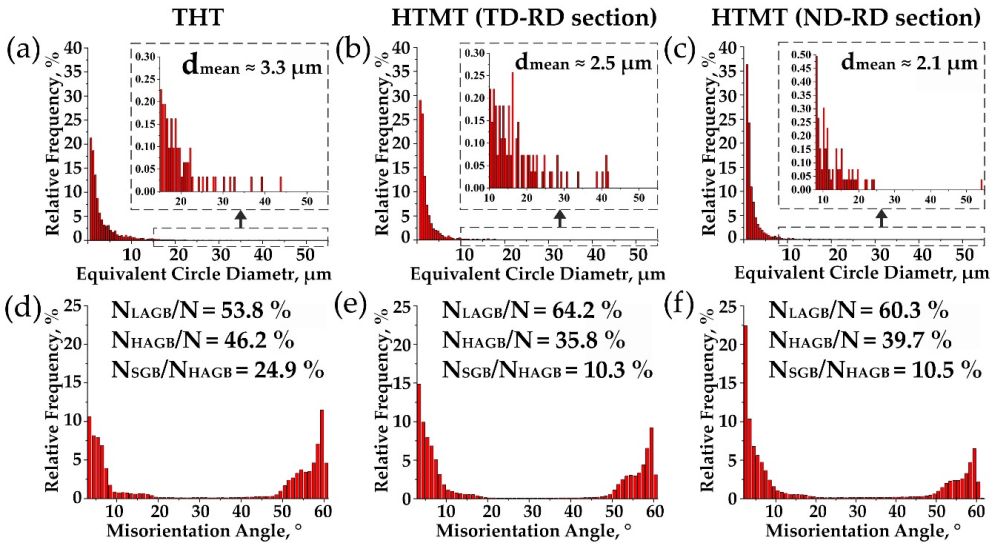

Figure 7. Grain misorientation distributions (**a**–**c**) and grain size distributions (**d**–**f**) after THT (**a**,**d**), HTMT in the section parallel to the rolling plane (TD-RD section) (**b**,**e**), and in the cross section (ND-RD section) (**c**,**f**). NLAGB/N, NHAGB/N, NSGB/NHAGB—fraction of low-angle, high-angle, and special boundaries (Σ 3), respectively.

The difference between the treatments is in the fraction of the smallest (≤2 μm) grains. After HTMT, both in the section parallel to the rolling plane and in the cross section, there is a tendency to refinement of martensite blocks and ferrite grain sizes (Figure 7a–c), in contrast to the THT case. In particular, after THT their average size (d_{mean}) is ≈3.3 μm, while after HTMT they decrease to 2.5 μm in the TD-RD section and to 2.1 in the ND-RD section, respectively.

As can be seen from Figure 7d–f, the distribution of grains over misorientation angles is bimodal for both studied treatments. There are two peaks corresponding to small-angle (<15°) and twin (or close to them, ≈60°) misorientations. Such a distribution is characteristic for ferritic-martensitic structures [29]. The first peak reflects the developed substructure of the material. The second peak corresponds to the boundaries of blocks and packets. Its appearance is associated with the features of the martensitic transformation as a shear phase γ-α transformation [30].

Practically no misorientations in the range from 20 to 50° in the studied steel are formed (Figure 7d–f). According to [30], this confirms the absence of polygonization processes during steel tempering and evidences of the formed microstructure stability.

It can be seen from Figures 6 and 7 that HTMT leads to an increase in the number of low-angle boundaries compared to THT. For instance, after THT their fraction is 53.8%, and the fraction of high-angle boundaries is 46.2%. After HTMT, in a section parallel to the rolling plane, the fraction of low-angle boundaries is 64.2%, and the fraction of high-angle boundaries is 35.8%. In the cross section, their percentage contents are 60.3 and 39.7%, respectively (Figures 6a–c and 7d–f). It is also worth noting an approximately

2-fold decrease, relative to the THT, in the fraction of special (with a misorientation of ≈60°) boundaries as a result of HTMT (from 24.9% to 10.3–10.5%, Figure 6a–c).

Figure 6j–l shows the distribution maps of geometrically necessary dislocations (GND) in steel EK-181 after THT and HTMT. A color gradient is observed on them, indicating an increase in their density, mainly near the grain and subgrain boundaries. As can be seen from Figure 6, after HTMT there is an increase in the specific density of boundaries, in comparison with THT. This also leads to an increase in the density of geometrically necessary dislocations (Figure 6j–l). The calculated average density of GND after THT is ≈9.0 × 10^{14} m^{-2}, after HTMT it reaches ≈10.9 × 10^{14} m^{-2} and ≈13.3 × 10^{14} m^{-2} in the TD-RD and ND-RD sections, respectively. The total scalar dislocation density is the sum of the density of geometrically necessary dislocations and statistically stored dislocations [22], the fraction of which is not taken into account by this method. GNDs are needed to maintain continuity between the grains. They determine the deformation inhomogeneity and its gradients, as well as the internal stress fields in the material [22].

The lower grain size identification limit is related to the scan step. In this regard, it should be noted that with the used parameters, not all boundaries of structural elements may be detected. The fine microstructure of the steel can be studied in more detail by transmission electron microscopy.

3.4. TEM Analysis

TEM studies have shown (Figure 8) that the structural-phase states of steel EK-181 after traditional heat treatment and high-temperature thermomechanical treatment (in a section parallel to the rolling plane) are qualitatively similar. After both treatments, a typical ferritic-martensitic microstructure is formed (the structure of a tempered lath martensite), dispersion-hardened by particles of second phases that differ in composition, size and spatial distribution (Figure 8).

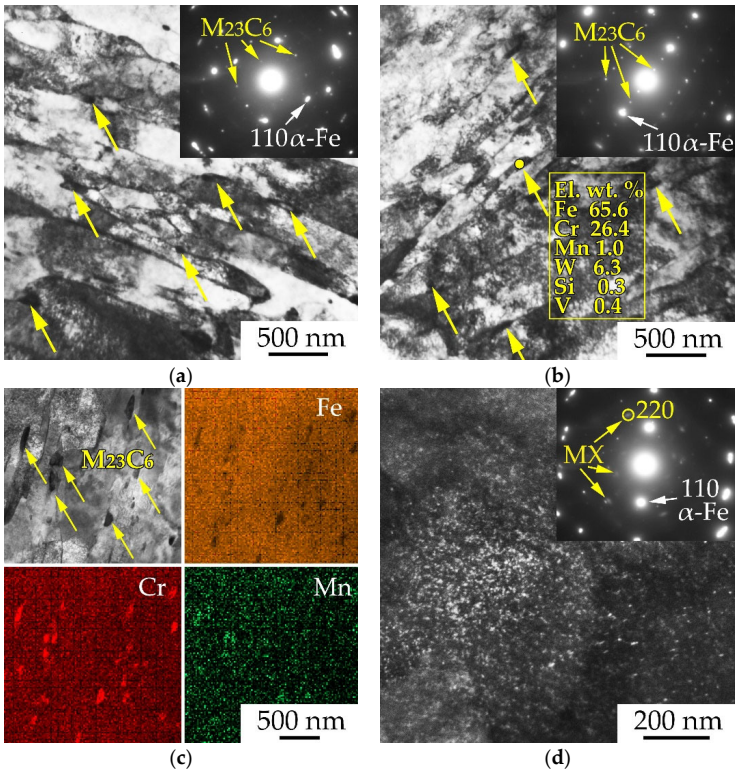

Figure 8. TEM images of steel microstructure after THT (**a**) and HTMT in a section parallel to the rolling plane (**b**–**d**): bright field (BF) images (**a**,**b**) with the corresponding micro diffraction (MD) patterns, scanning transmission electron microscopy (STEM) image with EDX elemental maps (**c**), dark field (DF) image in the reflection of MX-type carbonitrides (**d**).

The width of martensitic lamellae in the considered states varies from 100 to 700 nm (Figure 8a,b). Their average values after THT are ≈300 nm, after HTMT they are about 200 nm. The ferrite grains have a size of ≈1–3 μm after both treatments.

A fairly high dislocation density is observed in the steel microstructure (Figure 8a,b). According to TEM data, in the THT state, the dislocation density values can reach ≈(15–17) $\times$ 10^{14} m^{-2} in martensite regions and ≈(1–2) $\times$ 10^{14} m^{-2} in ferrite regions. As a result of HTMT, these values increase to ≈(16–18) $\times$ 10^{14} m^{-2} and ≈(3–4)$\times$ 10^{14} m^{-2}, respectively.

In accordance with the results of the analysis of microdiffraction patterns and elemental energy dispersive (EDX) microanalysis, relatively coarsely dispersed (from ≈50 to 400 nm in size) precipitates are the particles of $M_{23}C_6$ carbides based on Cr and Mn (Figure 8a–c). They mainly have a non-equiaxedshapes and are located along the boundaries of structural elements. Numerous authors report [6,13,16,17,21] that most of these particles are formed during the steel tempering. After THT, the dimensions of most $M_{23}C_6$ carbides are ≈100 nm. As a result of HTMT, they decrease to ≈ 80 nm. In addition, HTMT leads to a decrease in their volume fraction [17,21].

The second type of the observed particles is nanosized (5–10 nm) particles of the MX-type phase (M–V, Ti, Ta, etc., X–C, N) (Figure 8d). They are uniformly distributed in the body of the matrix grains predominantly on dislocations. By pinning the dislocation substructure of the steel, they reduce the effects of martensite tempering [21,31].

It was established in [17] that the HTMT of EK-181 steel leads to a higher dispersion and a larger volume fraction of these nanosized particles, in comparison with THT. As shown in [10,14,17,21], the precipitation of these particles in the HTMT mode can occur directly during hot plastic deformation of the austenite and its subsequent quenching. The high dislocation density caused by deformation in the austenite temperature range contributes, firstly, to a decrease in the nucleation barrier and the critical size of the new phase nuclei; secondly, an increase in the particle growth rate due to the higher diffusion coefficients on dislocations [17,21]. On the contrary, in the THT mode they precipitate mainly during high-temperature tempering [17].

Thus, the main differences between the treatments observed by TEM are the reduction in the transverse dimensions of the martensitic lamellae, a higher dislocation density, a larger volume fraction of the finely dispersed MX particles, and a smaller size and volume fraction of $M_{23}C_6$ carbides as a result of HTMT compared to THT. The latter, is apparently associated with a more intense, relative to THT, depletion of the solid solution in carbon during the formation of nanosized MX particles during plastic deformation in the austenite phase [17].

3.5. Tensile and Impact Properties

Figure 9a,b presents the curves of the temperature dependence of short-term tensile mechanical properties of EK-181 steel (yield strength—$\sigma_{0.2}$ and relative elongation to failure—δ) in the range from −196 to 800 °C after traditional heat and high-temperature thermomechanical treatments. A detailed description of the characteristic segments of these curves is given in [26,32]. As can be seen from this figure, HTMT leads to an increase (by ≈20%), relative to THT, in the yield strength of the steel in almost the entire temperature range under study, with a slight decrease in plasticity [32].

Figure 9c shows the engineering stress-strain curves for the THT and HTMT samples, subjected to tension loading at room and elevated (T = 650 °C) temperatures—near the upper limit of the would-be operating temperatures of the steel in the reactor core. When analyzing these curves, it was found out that in addition to higher strength properties (yield strength and ultimate tensile strength), HTMT results in a higher degree of strain hardening in the initial stage of the steel plastic deformation.

The yield strength of the steel after HTMT at 700 °C (≈305 MPa, Figure 9) corresponds to that after THT at 650 °C. This indicates a possibility of extending (by using HTMT) the temperature range of steel applicability to the region of elevated temperatures.

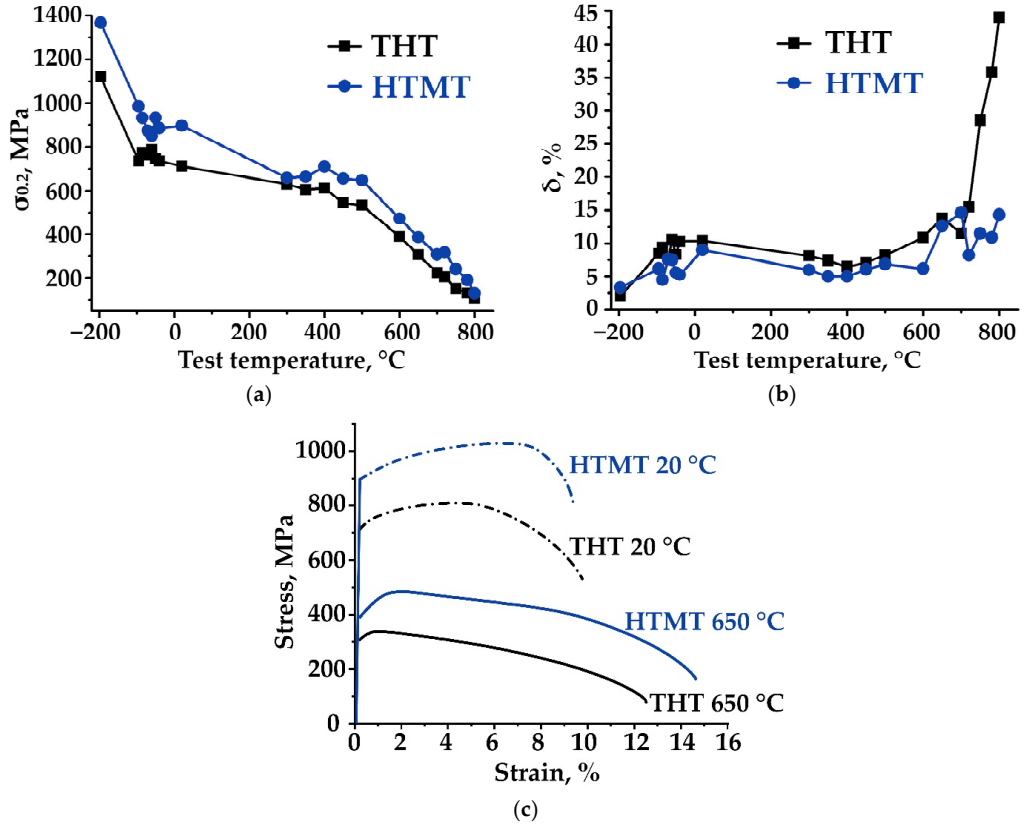

Figure 9. Tensile properties of EK-181 steel after THT and HTMT: curves of temperature dependence of yield strength (**a**) and relative elongation to failure (**b**), engineering stress-strain curves of samples tested at 20 and 650 °C (**c**).

The results of Charpy impact tests of the steel EK-181 samples in the temperature range from 100 to −186 °C in the THT and HTMT states are shown in Figure 10a. As can be seen from this figure, HTMT provides an increase, in comparison with THT, in the impact toughness of the steel at almost all considered temperatures.

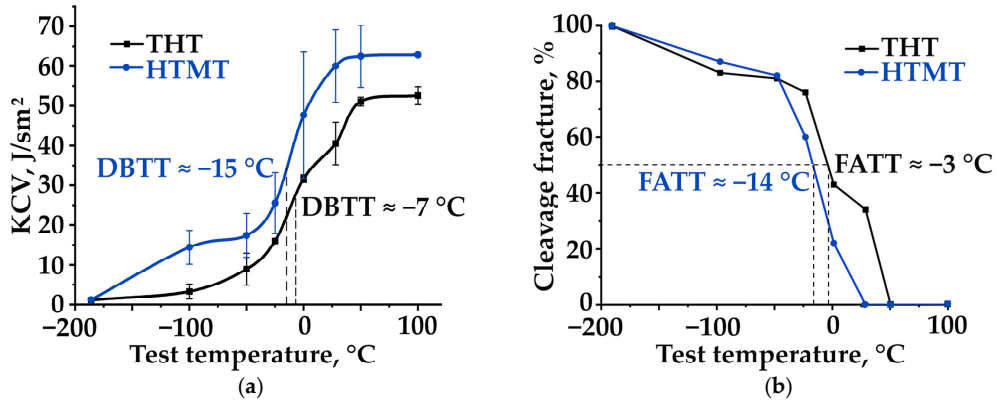

Figure 10. Temperature dependences of impact toughness (**a**) and brittle fracture (**b**) of steel EK-181 after THT and HTMT in the temperature range from 100 to −186 °C. DBTT—Ductile-Brittle Transition Temperature. FATT—Fracture Appearance Transition Temperature.

The upper shelf energy (at T = 50–100 °C) of the steel after THT is ≈54 J/cm^2, after HTMT—≈65 J/cm^2 (Figure 10a). Reducing the test temperature leads to a decrease in impact strength. Its drop to almost zero after both treatments was found in the region of cryogenic temperatures (T = −186 °C).

In addition, there is a decrease in the ductile-brittle transition temperature (DBTT) of the steel after HTMT (DBTT ≈ −15 °C) by several degrees, compared with THT (DBTT ≈ −7 °C) (Figure 10a). The impact strength (Charpy V-notch energy) at these temperatures has values of KV ≈ 28 J/cm^2 and ≈33 J/cm^2 after THT and HTMT, respectively [26].

3.6. Fractography

To establish a relationship between the values of the impact strength of the steel and the mechanism of its fracture, we carried out fractographic investigations of steel EK-181 impact samples after THT and HTMT, fractured in the temperature range from −186 to 100 °C. These studies have shown that the type of fractures is significantly affected both by the test temperature and the treatment mode.

At the temperatures corresponding to the upper shelf of the impact toughness temperature dependence, after both treatment modes, steel EK-181 fractures according to the mechanism of transcrystalline ductile fracture (Figure 11a–c). Since micropores (dimples) originate on inhomogeneities (second-phase particles, segregations of dissolved elements, grain boundaries), the size and distribution of the latter have a significant effect on the development of this type of fracture [18,20].

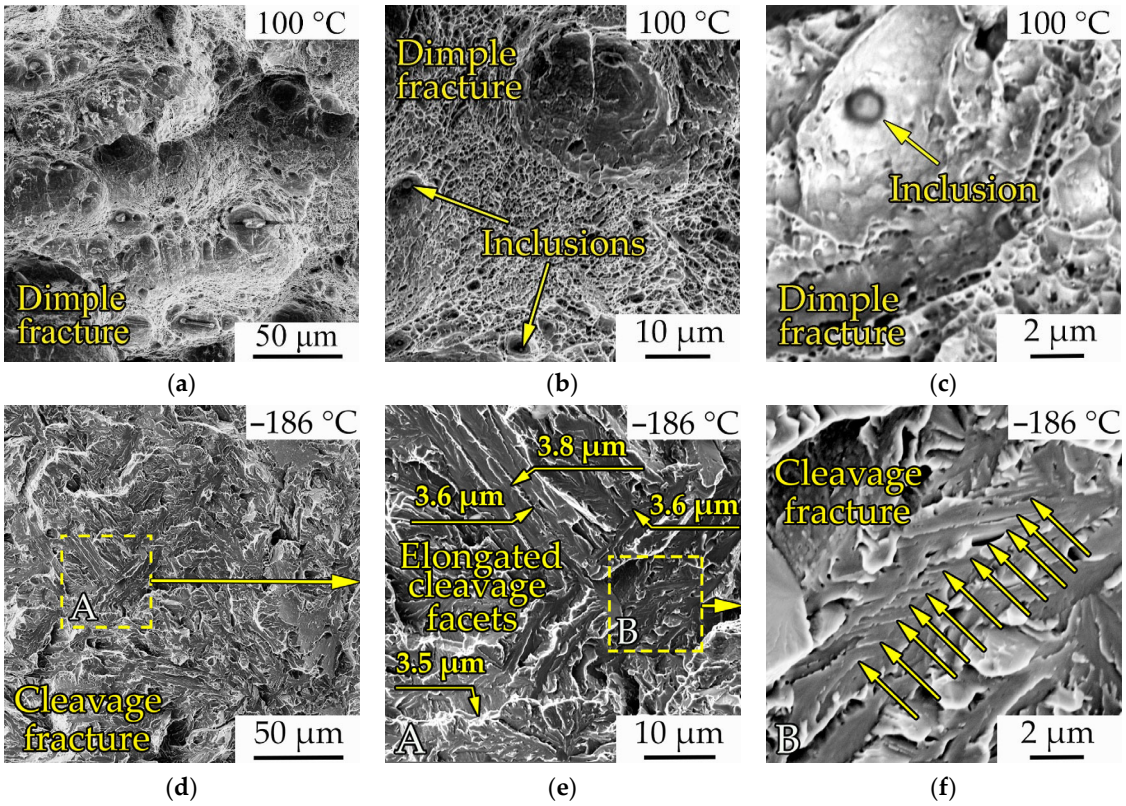

Figure 11. Fractographic images of the central part of steel EK-181 impact samples after THT, fractured at 100 °C (**a**–**c**) and −186 °C (**d**–**f**). Sections A and B highlighted by dotted rectangles are shown in Figures (**e**,**f**).

With a decrease in the test temperature—in the range of ductile-brittle transition—a zone of unstable crack propagation appears and increases in size (Figure 12). In this zone, the fracture is carried out by the mechanism of transcrystalline (in relation to the grain boundaries of the prior austenite, martensite packets and ferrite grains) quasi-cleavage with elements of brittle intercrystalline fracture (Figure 12a,c). The signs of both ductile and brittle fracture present in the steel indicates a mixed character of fracture in the temperature

range under discussion. It should be noted that HTMT leads to a decrease, in comparison with THT, the temperature, at that area of brittle fracture appears.

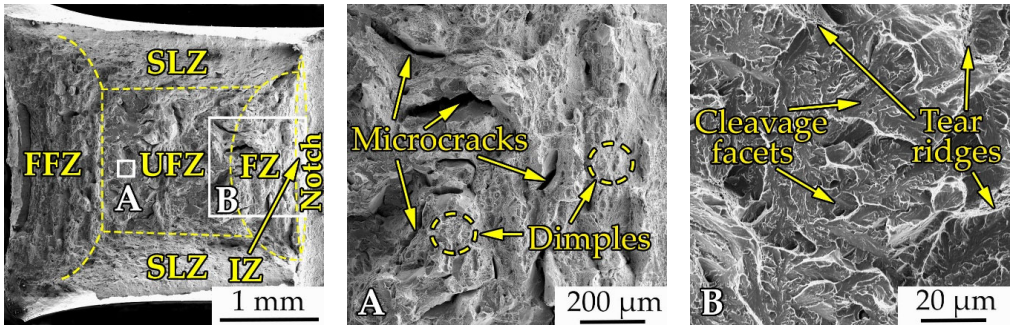

(**a**) (**b**) (**c**)

Figure 12. SEM images of fracture surface samples after THT after impact test at 28 °C (**a**) and magnified areas marked by white squares at a (**b**,**c**). IZ—crack initiation zone, FZ—fibrous zone, UFZ—unstable fracture zone, SLZ—shear lip zone, FFZ—final fracture zone.

When the temperatures corresponding to the lower shelf energy are reached, the zone of unstable crack propagation occupies almost the entire fracture surface, the areas of ductile fracture disappear—the steel fractures by the mechanism of transcrystalline quasi-cleavage. Fracture surfaces consist of numerous quasi-cleavage facets of various shapes and sizes. The dimensions (width) of the facets do not generally exceed ≈10 μm (Figure 11d–f). There are also elongated facets with transverse dimensions of about 4 μm are (Figure 11e), which can be correlated with the shape and size of martensite blocks (according to the EBSD data). On Figure 11f the arrows indicate periodically located steps. They might have been formed during propagation of a quasi-cleavage crack from one martensite lamella (or block) to another.

The ductile and brittle fracture areas were estimated at different impact test temperatures (Figure 10b). As can be seen from Figure 10b, the FATT temperature of steel EK-181 after THT and HTMT, at which these areas are equal, is close to the ductile-brittle transition temperature (DBTT) determined from the results of impact tests (Figure 10). So the value of FATT for the state after THT is ≈−3 °C, and after HTMT—≈ −14 °C (Figure 10b). Thus, the change in the fracture mechanism of the steel after HTMT occurs at lower temperatures relative to THT.

Another important difference in the structure of fractures after HTMT, in comparison with THT, is the formation in a temperature range of the ductile-brittle transition of steel delaminations in planes parallel to the rolling plane (RD-TD plane), specifically, perpendicular to the main crack propagation direction (Figure 13b).

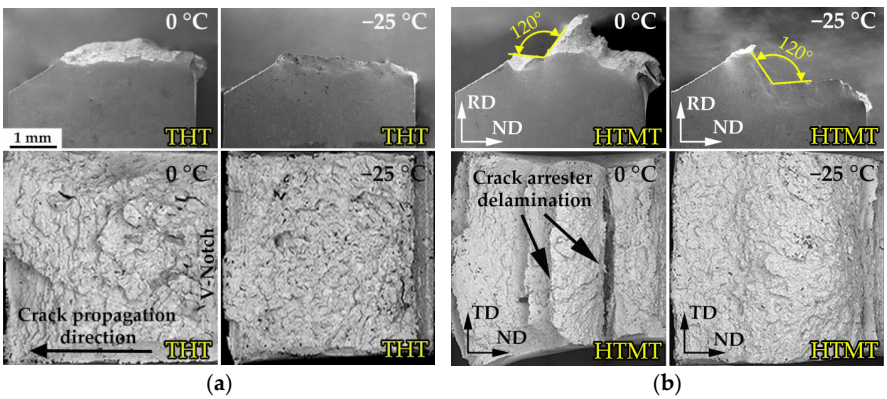

(**a**) (**b**)

Figure 13. SEM images of the lateral and fracture surfaces of steel impact samples after THT (**a**) and HTMT (**b**) fractured at 0 and −25 °C.

As can be seen from Figure 14, the delamination crack length can reach ≈800 μm. Encountering delaminations, the main crack can deviate (Figures 13b and 14) and propagate in a zigzag manner. The crack branching angle is most often ≈90° or ≈120° (Figures 13b and 14).

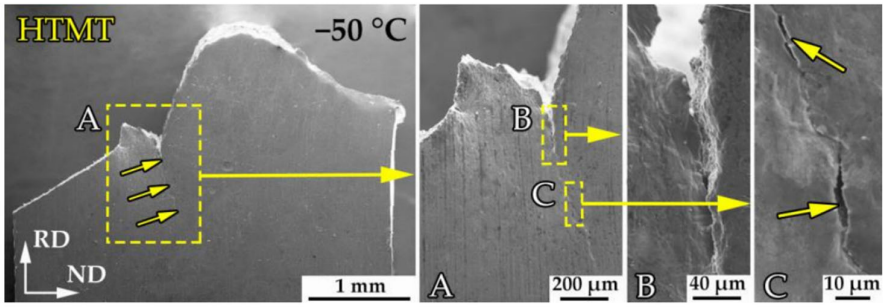

Figure 14. SEM images of the lateral surface of the impact sample after HTMT tested at −50 °C. A, B, C—magnified images of the areas outlined by dashed frames.

After THT, the main crack propagates along an almost straight path. No delaminations are formed in this case (Figure 13a).

Figure 15 a shows the etched side surface of the EK-181 steel sample (in the HTMT condition) after Charpy impact tests at T = −25 °C in the area of the main crack initiation and unstable propagation. The teeth on the fracture profile correspond to the crack branches. As can be seen from the figure, these deviations occur when the crack approaches the grain boundaries.

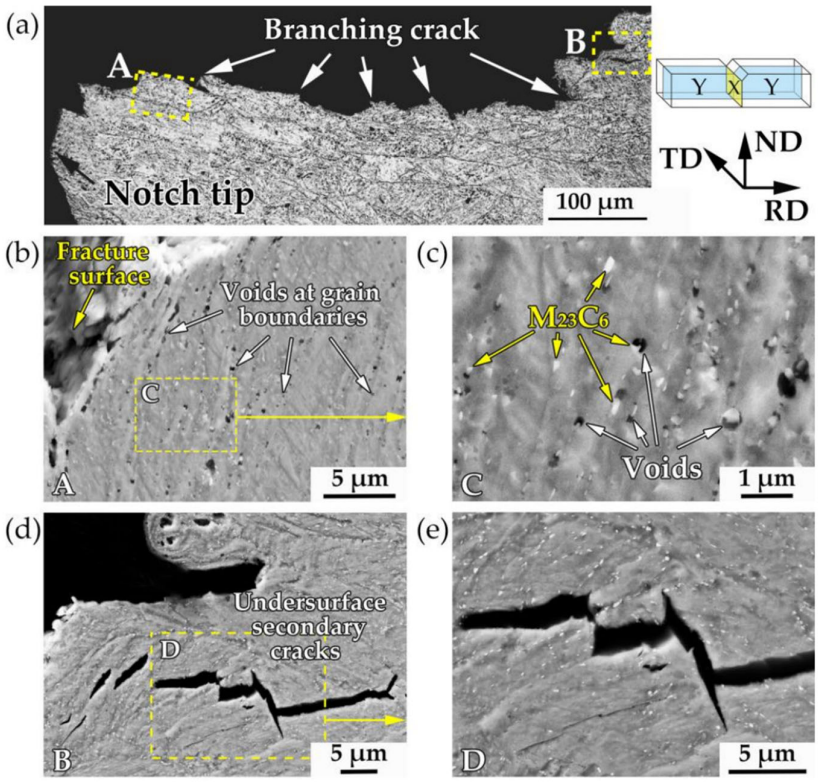

Figure 15. OM (**a**) and SEM (**b**–**e**) images of side surface of impact sample after HTMT, which fractured at T = −25 °C. The magnified images of the areas A–D outlined by dashed frames are represented in (**b**–**e**), respectively. X—fracture plane (yellow), Y—plane under investigation (light blue).

Near the fracture surface, we observed an active formation of pores lined up along straight lines (Figure 15b). A high-magnification examination showed (Figure 15c) that the

pores are formed on the particles of $M_{23}C_6$ carbides, which are located at the boundaries of the structural elements of the steel—prior austenite grains, packets, blocks and martensite lamellae. The accumulation of dislocations in front of strong carbide particles is likely to lead to an intense pore formation. It contributes to the relaxation of elastic stresses, that arise during loading.

In addition, there are secondary microcracks with a length of ≈2 to 40 μm, located under the fracture surface (Figure 15d,e). These cracks are non-linear. They have a zigzag shape, which might imply their branching on hitting the obstacles. According to [18], the delamination cleavage can initiate on parallel cleavage {100} planes lying almost parallel to the rolling plane. The secondary microcracks discussed here probably originate before the front of the propagating main crack, then they can merge with it or become blunt/stop before reaching their critical size.

4. Discussion

The results of structural investigations indicate that high-temperature thermomechanical treatment of ferritic-martensitic steel EK-181 leads to a significant modification of its structural-phase state, compared with traditional heat treatment. This causes the following:

1. A change in the shape and size of grains of the prior austenite. As a result, the HTMT forms a pancake structure. PAG grains become non-equiaxed: they are elongated in the rolling direction and flatten in the rolling plane. At the same time, in the rolling plane (ND-RD plane), their average sizes (diameter ≈128 μm) increase in comparison with the sizes of equiaxed grains after THT (diameter ≈100 μm). In the longitudinal section (TD-RD plane), the transverse dimensions of the PAGs are significantly (several times) reduced and become as small as ≈15 μm.
2. A decrease (by a factor of ≈1.5) in the sizes of martensite blocks and ferrite grains (up to 2.1–2.5 μm) separated mainly by high-angle boundaries. After THT, their average size is ≈3.3 μm.
3. An approximately 1.5-fold increase in the fraction of the smallest (≤2 μm) grains, which is most pronounced in the longitudinal section (TD-RD plane).
4. A more intensive formation of substructure elements (increase in the relative content of low-angle boundaries)—martensitic lamellae and subgrains of predominantly deformation origin with low-angle boundaries.
5. A decrease (by a factor of ≈1.5) in the width of martensite lamellae. Their mean values are ≈200 nm and 300 nm after HTMT and THT, respectively.
6. An increase in the density of dislocations by several times. The density of dislocations determined by different methods (SEM EBSD, TEM) differs. However, there is a general trend towards its increase after HTMT.
7. An increase in the volume fraction of vanadium-based carbonitrides of the MX type and a decrease in the size and volume fraction of relatively coarse $M_{23}C_6$ particles by about 1.2 times (from ≈6.2% after THT to ≈5.4% after HTMT).

Thus, as a result of HTMT, there is a refinement, relative to THT, of all elements of the grain-subgrain structure of steel EK-181. As discussed above, its structural elements are hierarchically organized. In this case, the refinement of austenite grains causes a change in the size of the remaining structure (martensite packets, blocks, ferrite grains) and substructure (martensite lamellae) elements.

In addition to the geometric factor of flattening of austenite grains, hot deformation of steel during HTMT contributes to an increase in the defectiveness of the material and the formation of new misorientation boundaries. These are predominantly low-angle boundaries separating the elements of the steel dislocation substructure. In addition, a certain number of grains of deformation origin with high-angle misorientations are likely to form, the boundaries of which are not boundaries of a special type.

In addition, a decrease in the size of austenite grains and the creation of additional stresses in it during hot rolling can reduce the temperature of the martensite transformation start (M_s). It also contributes to the refinement of the microstructure formed after this

transformation [33]. The precipitation of MX particles directly in the austenite can be an additional factor in reducing the M_s temperature [6].

Similar results were obtained in numerous works [5,6,10,13,14,16,25,29,34] studying the effect of hot rolling on the microstructure and carbide subsystem of 9–12% chromium ferritic-martensitic steels.

As noted earlier [20,34,35], for heat-resistant steels, an important role is played by their simultaneous dispersion (by thermally stable nanosized MX particles) and substructural (due to highly defective finely dispersed martesnitic structure) hardening. HTMT according to the proposed mode, due to the modification of the steel EK-181 microstructure, makes it possible to increase the efficiency of these hardening mechanisms. It provides a significant (by ≈20%) increase in its strength properties, compared with traditional heat treatment, in a wide temperature range from −196 to 800 °C (Figure 9).

It is known [21,36] that the glide stress (the Peierls-Nabarro stress) in BCC metals is higher compared to that of the FCC metals due to an asymmetric stress distribution around a dislocation. In addition, the Peierls-Nabarro stress is sensitive to the temperature. Apparently, this is one of the reasons for the found strong temperature dependence of the yield strength of steel EK-181 in the region of negative temperatures (Figure 9a).

Simultaneously with an increase in the yield strength of the steel, HTMT also contributes to an increase in its USE (upper shelf energy) and a decrease, relative to THT, in the ductile-brittle transition temperature by several degrees (from ≈−7 to −15 °C) (Figure 10).

It is believed [21,27,28,37] that the values of the impact strength of metallic materials correlate with the grain size. It has been experimentally shown in many works [12,27,37] that with a decrease in the effective grain size, it is possible to increase the impact toughness. However, in the study of multilevel ferritic-martensitic structures, there is an ambiguity about what to take as the effective grain size.

It has been reported [28] that low-angle boundaries (LABs) are ineffective arresters of cleavage crack propagation, while high-angle boundaries (HABs) deviate or retard crack propagation depending on the misorientation angle. In this case, the effective grain size can be taken as a crystallographic unit along which the cleavage crack propagates continuously.

The embrittlement of steel with decreasing temperature is reflected in the change in the fracture mechanism from ductile dimple transcrystalline fracture to brittle fracture by the mechanism of transcrystalline quasi-cleavage, which consumes much less energy (absorbs less energy) under impact loads.

The cleavage planes in ferritic-martensitic steels, being BCC materials, are the {001}-type planes, along which interatomic bonds break (via decohesion) during brittle fracture [17,21,28,38]. The effective grain size is the coherence length on {100} planes, which determines the cleavage crack length. Moreover, for the elongated grain structure, the coherence length on {100} planes is longer in the RD than in the transverse directions due to the elongated grain shape [38]. In the case of lath martensitic steels, the {100} coherence length is taken to be the size of martensite blocks, which are the basic crystallographic units [12]. According to [12], the microcracks formed inside martensite laths would join together to create a crack of a critical length to propagate as a cleavage crack.

Grain boundaries are the obstacles for the propagation of quasi-cleavage cracks [13,28,38]. When crossing high-angle boundaries (boundaries of blocks, packets), the crack may deviates or even stop [13,38]. Consequently, with an increase in the number of obstacles, the energy consumption of the destruction process increases. In addition, the orientation of the cleavage planes relative to the fracture surface has an effect on the cleavage crack propagation [28,36]. Different types of the cleavage planes distribution can cause the toughness anisotropy.

Thus, the cleavage facet size determines the steel resistance to the cleavage crack propagation and correlates with the dimensions of the steel structural elements. The smaller the facet size, the higher the resistance to cleavage fracture [28]. According to [21], the grain refinement also leads to a decrease in the stress concentration at grain boundaries and at triple junctions.

With regard to the above, one of the most important factors in increasing the impact toughness of EK-181 steel after HTMT, in our opinion, is the formation of an ultrafine grained structure in it.

In addition, the fractographic studies have shown that EK-181 steel after HTMT tends to form cracks propagating in the planes parallel to the rolling plane (perpendicular to the main fracture plane) during impact toughness tests in the ductile-brittle transition temperature range. This type of fracture is referred to in the literature as delamination, splitting, separation or fissures [12,17,22,23,26,28,34,38,39]. After THT, no such effects are observed.

Given the orientation of the V-notch with respect to the rolling plane (or with respect to the elongated grain structure) considered in this work, the resulting delaminations are classified as crack arrester-type delamination [22,23]. When crossing with the main crack, they can deflect it at an angle of up to 90° (up to 90°). Facilitating the branching of the main crack, delamination slows down its propagation in the impact direction.

The stress distribution in front of the notch is also of great importance, since it can control the fracture mechanism [22]. If the maximum achievable pre-notch stress is below the critical stress required for cleavage fracture, ductile fracture occurs rather than brittle quasi-cleavage fracture.

According to [22], delamination in the crack arrester orientation relaxes the triaxial stress condition at the crack tip, interrupting the main crack propagation. In this case, the fracture of the material requires repeated nucleation of a crack, which occurs under conditions of an almost uniaxial stress state. In this case, fracture by a quasi-cleavage manner is difficult.

Thus, the appearance of delaminations in EK-181 steel after HTMT leads to crack blunting and deflection, which consumes a lot of energy and enhances the impact energy dissipation [34]. The refined pancake microstructure formed as a result of hot rolling and subsequent tempering of steel EK-181 is effective for improving its toughness. In this case, not only the size, but also the shape of the formed elements of the grain-subgrain microstructure is of great importance.

The presence of delaminations of hot-rolled BCC steels and alloys during Charpy impact testing is widely reported in the literature [12,17,22,23,26,28,34,35,38,39]. Anisotropy of the impact strength value is found depending on the orientation of the rolled samples (the position of the V-notch) relative to the direction and plane of rolling [22,23] and, consequently, the type of delaminations formed. It was shown in [23] that the presence of delaminations plays a key role in this case. The highest impact strength values are demonstrated by the samples in which delaminations of the crack arrester type are formed (similar to those used in this work) [23,40].

Many authors note that the main reason for the appearance of delaminations is the anisotropy of the banded structure formed during hot rolling of ferritic-martensitic steels and the presence of relatively weak interfaces between the grains and subgrains elongated in the rolling direction [22,23,28,38–40]. In addition, the formation of a crystallographic texture and the segregation of impurities (for example, S and P atoms), and the coarsening of the secondary phase particles at grain boundaries can also contribute to material separation [23,40]. According to [22], delamination toughening is controlled by the ultrafine grain size, the grain shape and the <110> || RD fiber deformation texture.

A decrease in the size and volume fraction of $M_{23}C_6$ carbides after HTMT compared to THT can also have a positive effect on the value of the impact toughness of EK-181 steel. At elevated test temperatures (on the upper shelf energy), the second phase particles are the sites of predominant nucleation of micropores (ductile fracture dimples). At low test temperatures, they can initiate quasi-cleavage cracks, since the stress required to propagate a crack through the particle-matrix interface is inversely proportional to the square root of the particle size [21]. Therefore, reducing the density of large particles can be an effective way to increase the absorbed fracture energy of the steel at low temperatures.

Thus, the use of HTMT for low-activation ferritic-martensitic steel EK-181 due to the refinement of the grain and carbide structure and delamination toughening makes it possible to obtain an optimal combination of its strength and plastic properties (including in the high-temperature region) and acceptable values of impact toughness at reduced temperatures.

5. Conclusions

1. High-temperature thermomechanical treatment of low-activation ferritic-martensitic steel EK-181 with deformation in the austenitic region leads to the formation of pancake structure. In this case, all hierarchically organized structure of the material is refined. The transverse dimensions of the prior austenite grains, packets, blocks and laths of martensite are reduced by about 1.5 times, compared with the traditional heat treatment of this steel.
2. HTMT affects the defect substructure of the steel. It contributes to an increase, relative to THT, in the dislocation density and the formation of new predominantly low-angle misorientation boundaries, both due to the refinement of martensite lamellae and due to the creation of deformation-induced subboundaries.
3. Another most important effect of HTMT is a change in the parameters of the carbide subsystem of EK-181 steel. HTMT due to the redistribution of carbon between precipitated particles of the second phases leads to an increase in the dispersion of nanosized thermally stable particles of MX type carbonitride mainly based on V and a simultaneous decrease in the size and volume fraction of relatively coarsely dispersed $M_{23}C_6$ carbides, compared with THT.
4. The elongated ultrafine-grained highly defective microstructure formed as a result of HTMT with a high density of nanosized particles, due to the increase in the efficiency of joint dispersion and substructural hardening, provides a noticeable increase (by ≈20%), relative to THT, in the yield strength of EK-181 steel in a wide temperature range from −196 up to 800 °C.
5. An increase in the impact toughness of steel EK-181 after HTMT and a slight decrease in the ductile-brittle transition temperature are mainly due to the refinement of its grain-subgrain microstructure and carbide subsystem, as well as to the formation of delaminations in the planes parallel to the rolling plane.

Author Contributions: Conceptualization, N.P. and I.L.; methodology, N.P.; formal analysis, E.M. and V.L.; investigation, N.P., V.L., K.A., S.A., E.M., N.D. and K.M.; resources, V.C.; writing—original draft preparation, N.P.; writing—review and editing, N.P., I.L., V.C. and M.L.-S.; visualization, S.A., K.A. and V.L.; supervision, V.C. and M.L.-S.; project administration, N.P. All authors have read and agreed to the published version of the manuscript.

Funding: This study was funded by the Russian Science Foundation; Project No. 21-79-00231, https://rscf.ru/en/project/21-79-00231/, accessed on 8 November 2022.

Acknowledgments: The research was carried out with the equipment of Tomsk Regional Core Shared Research Facilities Center of National Research Tomsk State University (center was supported by the Ministry of Science and Higher Education of the Russian Federation) and Share Use Centre "Nanotech" of the ISPMS SB RAS.

Conflicts of Interest: The authors declare no conflict of interest.

References

1. Odette, G.R.; Zinkle, S.J. *Structural Alloys for Nuclear Energy Applications*; Elsevier: Amsterdam, The Netherlands, 2019; p. 655. [CrossRef]
2. Klueh, R.L.; Nelson, A.T. Ferritic/martensitic steels for next-generation reactors. *J. Nucl. Mater.* **2007**, *371*, 37–52. [CrossRef]
3. Leontieva-Smirnova, M.V.; Agafonov, A.N.; Ermolaev, G.N.; Ioltukhovsky, A.G.; Mozhanov, E.M.; Revisnikov, L.I.; Tsvelev, V.V.; Chernov, V.M.; Bulanova, T.M.; Golovanov, V.N.; et al. Microstructure and mechanical properties of low-activated ferritic-martensitic steel EK-181 (RUSFER-EK-181). *Perspect. Mater.* **2006**, *6*, 40–52. (In Russian)

4. Chernov, V.M.; Leonteva-Smirnova, M.V.; Potapenko, M.M.; Budylkin, N.I.; Devyatko, Y.N.; Ioltukhovsky, A.G.; Mironova, E.G.; Shikov, A.K.; Sivak, A.B.; Yermolaev, G.N.; et al. Structural materials for fusion power reactors—The RF R&D activities. *Nucl. Fusion* **2007**, *47*, 839–848.
5. Prakash, P.; Vanaja, J.; Srinivasan, N.; Parameswaran, P.; Nageswara Rao, G.V.S.; Laha, K. Effect of thermo-mechanical treatment on tensile properties of reduced activation ferritic-martensitic steel. *Mater. Sci. Eng. A* **2018**, *724*, 171–180. [CrossRef]
6. Shruti, P.; Sakthivel, T.; Nageswara Rao, G.V.S.; Laha, K.; Srinivasa Rao, T. The Role of Thermomechanical Processing in Creep Deformation Behavior of Modified 9Cr-1Mo Steel. *Metall. Mater. Trans. A* **2019**, *50*, 4582–4593. [CrossRef]
7. Zinkle, S.J.; Moslang, A. Evaluation of irradiation facility options for fusion materials research and development. *Fusion Eng. Des.* **2013**, *88*, 472–482. [CrossRef]
8. Samant, S.S.; Singh, I.V.; Singh, R.N. Effect of Thermo-mechanical Treatment on High Temperature Tensile Properties and Ductile–Brittle Transition Behavior of Modified 9Cr-1Mo Steel. *Metall. Mater. Trans. A* **2020**, *51*, 3869–3885. [CrossRef]
9. Chernov, V.M.; Ermolaev, G.N.; Leont'eva-Smirnova, M.V. Impact toughness of EK-181 ferritic-martensitic chromium (12%) steel under loading by concentrated bending. *Tech. Phys.* **2010**, *7*, 985–990. [CrossRef]
10. Zhou, J.H.; Shen, Y.F.; Xue, W.Y.; Jia, N. Hot-deformation induced static recrystallization and nano-MX precipitation in a low activation martensitic steel. *J. Nucl. Mater.* **2021**, *556*, 153190. [CrossRef]
11. Stornelli, G.; Schino, A.D.; Mancini, S.; Montanari, R.; Testani, C.; Varone, A. Grain Refinement and Improved Mechanical Properties of EUROFER97 by Thermo-Mechanical Treatments. *Appl. Sci.* **2021**, *11*, 10598. [CrossRef]
12. Tan, L.; Yang, Y.; Busby, J.T. Effects of alloying elements and thermomechanical treatment on 9Cr Reduced Activation Ferritic–Martensitic (RAFM) steels. *J. Nucl. Mater.* **2013**, *442*, S13–S17. [CrossRef]
13. Hollner, S.; Piozin, E.; Mayr, P.; Caës, C.; Tournié, I.; Pineau, A.; Fournier, B. Characterization of a boron alloyed 9Cr3W3CoVNbBN steel and further improvement of its high-temperature mechanical properties by thermomechanical treatments. *J. Nucl. Mater.* **2013**, *441*, 15–23. [CrossRef]
14. Klueh, R.L.; Hashimoto, N.; Maziasz, P.J. New nano-particle-strengthened ferritic/martensitic steels by conventional thermomechanical treatment. *J. Nucl. Mater.* **2007**, *367–370*, 48–53. [CrossRef]
15. Mao, C.; Liu, C.; Liu, G.; Yu, L.; Li, H.; Dong, J.; Liu, Y. The Correlation Between the Microstructural Parameters and Mechanical Properties of Reduced Activation Ferritic–Martensitic (RAFM) Steel: Influence of Roll Deformation and Medium Temperature Tempering. *Metall. Mater. Trans. A* **2021**, *52*, 119–128. [CrossRef]
16. Vivas, J.; Capdevila, C.; Altstadt, E.; Houska, M.; San-Martín, D. Importance of austenitization temperature and ausforming on creep strength in 9Cr ferritic/martensitic steel. *Scr. Mater.* **2018**, *153*, 14–18. [CrossRef]
17. Polekhina, N.A.; Litovchenko, I.Y.; Tyumentsev, A.N.; Kravchenko, D.A.; Chernov, V.M.; Leontyeva-Smirnova, M.V. Effect of high-temperature thermomechanical treatment in the austenite region on microstructure and mechanical properties of low-activated 12% chromium ferritic-martensitic steel EK-181. *Tech. Phys.* **2017**, *62*, 736–740. [CrossRef]
18. Mohrbacher, H. Property Optimization in As-Quenched Martensitic Steel by Molybdenum and Niobium Alloying. *Metals* **2018**, *8*, 234. [CrossRef]
19. Pineau, A.; Benzerga, A.A.; Pardoen, T. Failure of metals I: Brittle and ductile fracture. *Acta Mater.* **2016**, *107*, 424–483. [CrossRef]
20. Kuhn, H.; Medlin, D. *ASM Handbook: Mechanical Testing and Evaluation*; ASM International: Russel, OH, USA, 2000; Volume 8, p. 998. ISBN 978-0-87170-389-7.
21. Yin, S.; Liu, Y.; Zhao, F. Effect of thermomechanical treatment on MX phase precipitation behavior in CLAM steel. *Fusion Eng. Des.* **2021**, *173*, 112785. [CrossRef]
22. Kimura, Y.; Inoue, T. Influence of Warm Tempforming on Microstructure and Mechanical Properties in an Ultrahigh-Strength Medium-Carbon Low-Alloy Steel. *Metall. Mater. Trans. A* **2013**, *44*, 560–576. [CrossRef]
23. Haskel, H.L.; Pauletti, E.; Martins, J.P.; de Carvalho, A.L.M. Microstructure and microtexture assessment of delamination phenomena in charpy impact tested specimens. *Mater. Res.* **2014**, *17*, 1238. [CrossRef]
24. Hoffmann, J.; Rieth, M.; Commin, L.; Fernández, P.; Roldán, M. Improvement of reduced activation 9% Cr steels by ausforming. *Nucl. Mater. Energy* **2016**, *6*, 12–17. [CrossRef]
25. Litovchenko, I.; Almaeva, K.; Polekhina, N.; Akkuzin, S.; Linnik, V.; Moskvichev, E.; Chernov, V.; Leontyeva-Smirnova, M. The Microstructure and Mechanical Properties of Ferritic-Martensitic Steel EP-823 after High-Temperature Thermomechanical Treatment. *Metals* **2022**, *12*, 79. [CrossRef]
26. Polekhina, N.A.; Linnik, V.V.; Almaeva, K.V.; Litovchenko, I.Y.; Tymentsev, A.N.; Moskvichev, E.N.; Chernov, V.M.; Leontyeva-Smirnova, M.V.; Degtyarev, N.A.; Moroz, K.A. Effect of high temperature thermomechanical treatment on the tendency of low-activation 12% Cr ferritic-martensitic steel EK-181 to low temperature embrittlement. *Russ. Phys. J.* **2022**, *64*, 2225–2231. [CrossRef]
27. Li, X.; Lu, G.; Wang, Q.; Zhao, J.; Xie, Z.; Misra, R.D.K.; Shang, C. The Effects of Prior Austenite Grain Refinement on Strength and Toughness of High-Strength Low-Alloy Steel. *Metals* **2022**, *12*, 28. [CrossRef]
28. Chatterjee, A.; Ghosh, A.; Moitra, A.; Bhaduri, A.K.; Mitra, R.; Chakrabarti, D. Role of hierarchical martensitic microstructure on localized deformation and fracture of 9Cr-1Mo steel under impact loading at different temperatures. *Int. J. Plast.* **2018**, *104*, 104–133. [CrossRef]
29. Hannula, J.; Porter, D.; Kaijalainen, A.; Somani, M.; Kömi, J. Optimization of Niobium Content in Direct Quenched High-Strength Steel. *Metals* **2020**, *10*, 807. [CrossRef]

30. Lobanov, M.L.; Rusakov, G.M.; Redikultsev, A.A.; Belikov, S.V.; Karabanalov, M.S.; Struina, E.R.; Gervas'ev, A.M. Investigation of Special Misorientations in Lath Martensite of Low-Carbon Steel Using the Method of Orientation Microscopy. *Phys. Met. Metallogr.* **2016**, *117*, 254–259. [CrossRef]
31. Xu, Y.; Li, W.; Wang, M.; Zhang, X.; Wu, Y.; Min, N.; Liu, W.; Jin, X. Nano-sized MX carbonitrides contribute to the stability of mechanical properties of martensite ferritic steel in the later stages of long-term aging. *Acta Mater.* **2019**, *175*, 148–159. [CrossRef]
32. Polekhina, N.A.; Litovchenko, I.Y.; Almaeva, K.V.; Tymentsev, A.N.; Chernov, V.M.; Leontyeva-Smirnova, M.V. Microstructure, Structural-Phase Transformations, and Mechanical Properties of Low-Activation 12% Chromium Ferritic-Martensitic Steel EK-181 Depending on the Treatment Conditions. *Inorg. Mater.* **2022**, *13*, 1247–1260. [CrossRef]
33. Zhang, M.; Wang, Y.H.; Zheng, C.L.; Zhang, F.C.; Wang, T.S. Austenite deformation behavior and the effect to ausforming process on martensite starting temperature and ausformed martensite microstructure in medium-carbon Si–Al-rich alloy steel. Mater. *Sci. Eng. A* **2014**, *596*, 9–14. [CrossRef]
34. Maeda, T.; Okuhata, S.; Matsuda, K.; Masumura, T.; Tsuchiyama, T.; Shirahata, H.; Kawamoto, Y.; Fujioka, M.; Uemori, R. Toughening mechanism in 5%Mn and 10%Mn martensitic steels treated by thermo-mechanical control process. *Mater. Sci. Eng. A* **2021**, *812*, 141058. [CrossRef]
35. Honeycombe, R.W.K. *The Plastic Deformation of Metals*; Edward Arnold: London, UK, 1968; p. 477.
36. Modak, P.; Ghosh, A.; Rarhi, N.; Kumar, V.; Balamuralikrishnan, R.; Chakrabarti, D. A review on the effect of microstructure, texture and inclusion on Charpy impact transition behaviour of low-carbon ferritic steels. *Met. News* **2016**, *19*, 21–34.
37. Niu, Y.; Jia, S.; Liu, Q.; Tong, S.; Li, B.; Ren, Y.; Wang, B. Influence of Effective Grain Size on Low Temperature Toughness of High-Strength Pipeline Steel. *Materials* **2019**, *12*, 3672. [CrossRef]
38. Dudko, V.; Fedoseeva, A.; Kaibyshev, R. Ductile-brittle transition in a 9% Cr heat-resistant steel. *Mater. Sci. Eng. A* **2017**, *682*, 73–84. [CrossRef]
39. Mishnev, R.; Dudova, N.; Dudko, V.; Kaibyshev, R. Impact toughness of a 10% Cr steel with high boron and low nitrogen contents. *Mater. Sci. Eng. A* **2018**, *730*, 1–9. [CrossRef]
40. Ghosh, A.; Patra, S.; Chatterjee, A.; Chakrabarti, D. Effect of Local Crystallographic Texture on the Fissure Formation During Charpy Impact Testing of Low-Carbon Steel. *Metall. Mater. Trans. A* **2016**, *47*, 2755. [CrossRef]